Emergent Degradation Phenomena Demonstrated on Resilient, Flexible and Scalable Integrated Photoelectrochemical Cells

Tobias A. Kistler[1,2] and Guosong Zeng[1], James L. Young[3], Lien-Chun Weng[4,5], Chase Aldridge[3], Keenan Wyatt[3], Myles A. Steiner[3], Oscar Solorzano Jr.[1,5], Frances A. Houle[1], Francesca M. Toma[1], Adam Z. Weber[4], Todd G. Deutsch[3], Nemanja Danilovic[4,]*

[1] Chemical Sciences Division, Lawrence Berkeley National Laboratory, Berkeley, California, 94720.

[2] Walter Schottky Institute and Physics Department, Technische Universität München, Garching, Germany

[3] Chemistry and Nanoscience Center, National Renewable Energy Laboratory, Golden, Colorado, 80401.

[4] Energy Storage and Distributed Resources Division, Lawrence Berkeley National Laboratory, Berkeley, California, 94720.

[5] Department of Chemical and Biomolecular Engineering, University of California, Berkeley, California, 94720.

*corresponding author: ndanilovic@lbl.gov

Keywords

PEC cell scale-up, durability, reproducibility, on-sun testing, water splitting

Abstract

Photoelectrochemical (PEC) water splitting provides a pathway to generate sustainable clean fuels using the two most abundant resources on Earth: sunlight and water. Currently, most of the successful models of PEC cells are still fabricated on small scales near 1 cm^2, which largely limits the mass deployment of solar-fuel production. Here, the scale-up to 8 cm^2 of an integrated PEC (IPEC) device is demonstrated and its performance compared to a 1 cm^2 IPEC cell, using state-of-the-art iridium and platinum catalysts with III-V photoabsorbers. The initial photocurrents at 1 sun were 8 and 7 mA cm^{-2} with degradation rates of 0.60 and 0.47 mA cm^{-2} day^{-1}, during unbiased operation for the 1 and 8 cm^2 devices, respectively. Evaluating under outdoor and indoor conditions at two US National Laboratories revealed similar results, evidencing the reproducibility of this design's performance. Furthermore, the emerging degradation mechanisms during scale-up are investigated and the knowledge gained from this work will provide feedback to the broader community, since PEC device durability is a limiting factor in its potential future deployment.

1. Introduction

While electrification of light-duty vehicles in conjunction with increasing renewable electricity generation is promising in reducing global carbon dioxide (CO_2) emissions, deep decarbonization will require changes to food production, chemical industry, steel production, heating and heavy-duty transportation.[1] Hydrocarbons still dominate these sectors. However, hydrogen (H_2) poses an attractive CO_2 emission-free alternative if it is not obtained from steam methane reforming (SMR) or fossil-fuel-powered electrolysis. Water-splitting technologies offer multiple pathways to meet this demand if they can be scaled up and made more efficient to reduce the cost of produced hydrogen and compete with SMR ($1.25-3.50 kg^{-1}),[2][3] with an ultimate levelized cost target of $2 kg^{-1} for H_2 set by the U.S. Department of Energy (DOE).[4][5] Photoelectrochemical (PEC) water splitting is one of those pathways with the potential to produce low-cost hydrogen efficiently from water, using sunlight as the only other input.[6]–[8] Traditionally, PEC devices directly convert photons from the sun to H_2 on photoelectrodes with at least one photoabsorber/electrolyte junction, as opposed to photovoltaic-electrolysis (PV-E) in which a PV directly powers an electrolyzer, an electrochemical water-splitting device.[9]–[12] More recently, integrated PEC (IPEC) architectures have emerged.[13] IPEC devices separate the photoabsorber from the electrolyte, but keep them in close vicinity to each other (within the nm to μm range), alleviating some of the challenges imposed by the direct photoabsorber/electrolyte interfaces. Opposed to physically separated PV-E systems, IPEC architectures benefit from thermal coupling between the hot PV and cool electrolysis components. While PV devices work more efficiently at lower temperatures, water splitting reaction rates increase at higher temperatures.[14] In either case there is an anodic reaction (oxygen evolution), and a cathodic reaction (hydrogen evolution), generally separated by a membrane to isolate the products. There

are many vastly different PEC cell designs used for demonstrating material and device properties, hindering the establishment of clear standards such as were developed in the electrolyzer community.[8][11] Furthermore, most PEC studies and proposed devices consist of cells with less than 1 cm^2 active area, and use liquid electrolytes.[15]–[19] As we look towards scaling these cells up from 1 cm^2 to larger platforms, new strategies are required to overcome the disadvantages of a liquid electrolyte feed. A material conundrum to date is that durable materials show poor efficiency due to their wide bandgap (e.g. transition metal oxides), while efficient (III-V) materials suffer from thermodynamic instability in a wide range of liquid electrolyte, especially highly acidic or alkaline.[20]–[22] In addition to these degradation issues, water management and piping at scale becomes increasingly difficult as PEC cells increase in size. Recently, we proposed one solution which integrates the PV in a proton-exchange-membrane (PEM)-based electrolyzer.[23] This integrated PEC cell may be fed by liquid water or water vapor in combination with a solid polymer electrolyte, such as Nafion.[23]–[28] We demonstrated over 100 hours of steady solar-to-hydrogen (STH) efficiency under a combination of steady-state and diurnal simulated light.[23] There was no noticeable degradation of the Pt and Ir electrocatalysts or the photovoltaic (PV) when appropriate water management, to limit water contact with the PV, was employed. This integrated cell can be used as a test bed to evaluate photovoltaics, (photo-)catalysts, barrier coatings and different cell configurations to isolate the degradation sources. Herein, we describe a multiphysics modeling-driven scale-up of the IPEC cell from 1 cm^2 to 8 cm^2 active area to systematically explore emerging degradation mechanisms *at scales* that introduce thermal, bubble and water, kinetic and mass-transport issues that will be seen in panels used for MW-scale deployment, while keeping the electrochemically and photoactive materials constant. We integrate both commercially-available and NREL-grown III-V

semiconductors into our IPEC device platform demonstrating its modularity. Furthermore, we provide a pathway towards direct integration of electrochemical and barrier layer components during the PV fabrication process. We employ state-of-the-art PEM membranes and electrocatalysts. In order to stress the device concept and demonstrate the potential of this IPEC technology, we evaluate the durability under indoor and outdoor conditions at two U.S. National Lab locations with markedly different altitudes and local atmospheric characteristics: Lawrence Berkeley National Laboratory in Berkeley, California and the National Renewable Energy Laboratory in Golden, Colorado.

2. Results and Discussion

2.1 Integrated PEC (IPEC) cell design

The design of the cell is detailed in a previous publication.[23] Briefly, the design includes many facets incorporated from traditional, electrochemical, membrane electrode assembly (MEA)-based electrolyzers and fuel cells, which consist of endplates, flowfields, current collectors, and electrodes separated by an ion-conducting membrane.

The endplates are machined from polymethylmethacrylate (PMMA) and flow ports (green tubes perpendicular to the endplates in Figure 1a-b) are attached with epoxy in the holes of the plates. Upon tightening the screws, the endplates provide uniform compression of the cell components. Since the endplates are electrically insulating, conductive Ti foils with channels, serving multiple functions as current collectors, catalyst supports and flowfields, are added.

In the integrated device, the flowfields in front of the PV will have a shadowing effect (**Figure S1**), motivating the optimization of the flowfield land width. A multiphysics model

(**Figure S2** and **Table S1**) is employed to drive this optimization. Figure 1c shows the electrochemical (EC) and PV performance as a function of the land width. Varying the land width from 50 to 200 μm decreases the overpotential of the electrolyzer by 80 mV at the operating point. The decrease is due to the increased amount of catalyst in contact with the membrane and the lower operating current density due to increased PV shading, lowering its performance. As the current density is directly proportional to the efficiency of the device,[23] thicker lands will ultimately reduce the maximum efficiency. However, if the chosen width is too thin, the operating voltage may surpass the maximum power point of the PV as the catalytic area is decreased significantly.

We find that the catalyst closer to the edge of the land has a higher activity because of the lower ohmic resistances in those regions (**Figure S3**). Therefore, the current density could be increased without compromising shading by increasing the number of catalyst-coated lands while making them narrower. However, we found that this only resulted in a 2% increase in the total current going from 10 to 30 lands. Furthermore, thin lands in the range of 50 μm are fragile, difficult to machine and poor supports for the employed Nafion membrane, which electrically separates the two conductive flowfields. As a compromise between performance and mechanical stability, we chose a land width of 100 μm. This pattern maximizes the amount of light going through the cell, while still supporting the membrane and allowing for mass transport.

2.2 Reference cell calibration

Prior to performing any durability tests, we characterized reference cells and solar simulators available at LBNL and NREL extensively, and the cross-comparison is summarized in Error:

Reference source not found. At LBNL, a Si reference was used to position IPEC cells while at NREL, the primary GaInP reference cell was chosen. The results show that a multi-junction PV may be significantly over- or under-illuminated when light source calibration is performed without regard to the current-limiting junction and performing spectral correction. For example, an InGaAs subcell could be over-illuminated by 34% when positioned with a GaInP reference cell in front of the ABET solar simulator. In our case, external quantum efficiency data (data sheet from AZUR SPACE[29] and **Figure S4** for NREL PVs) show that the GaAs junction is current-limiting. In this case, the ABET simulator plus GaInP reference would over-illuminate the IPEC cell by 8%. Similarly, the Sol3A simulator plus Si reference results in 1% over-illumination. Thus, such method of light source calibration without spectral correction would yield photocurrents differing by 7%.

2.3 Indoor stability test

After assembling two IPEC devices, one with a 1 cm^2 NREL-made PV and the other one with an 8 cm^2 AZUR SPACE PV, we measure the initial performance and short-term durability of both. The characterization of the AZUR SPACE and NREL-made PVs can be found in Figure S4.

As shown in Figure 2a, the initial PV performance in the full assembly is very similar, but the maximum photocurrent in the 8 cm^2 device is slightly lower. The lower photocurrent is mainly due to the longer lands of the flowfields which tend to be less taut in the larger device, making it more difficult to align all anode and cathode lands across the membrane. In areas of misalignment, this likely causes longer proton transport distances and less intimate membrane-electrode contact, while increasing PV shading. The open-circuit voltage of the 8 cm^2 PV is

larger since it consists of three junctions opposed to the two-junction 1 cm^2 PV. The EC performance of the larger cell is slightly reduced, partially due to the lower ratio of catalyst to PV area in the larger cell (**Figure S5**). Furthermore, increased membrane swelling in the scaled-up device may reduce the catalytic area in contact with the membrane, lowering the EC performance.[30]

Both IPEC assemblies show good stability during an initial 1-hour assessment (Figure 2b). The measured current density of the IPEC cells equaled the short-circuit current density of the PV, and no degradation is visible. The operating voltage of the 8 cm^2 cell is slightly higher than the 1 cm^2 cell, as predicted from the intersections of the EC and PV curves in Figure 2a and is very stable in both cases. The good stability is in part enabled by feeding pure water, instead of the strongly acidic or basic electrolytes commonly used in (I)PEC devices.[31]–[39] While PEC devices often suffer from significant performance losses during scale-up (**Table S2**),[40]–[47] our initial assessments suggest that this IPEC device design is scalable without large performance losses and that the results are reproducible. Furthermore, we analyze the material costs of the device, indicating that light concentration may be necessary to offset today's high costs of low-volume III-V PVs and to achieve the DOE cost target (**Table S3** and **Table S4**).[48]–[51]

2.4 Outdoor stability test

After confirming the successful scale-up of the device architecture, we test the 8 cm^2 cell outdoors at LBNL and NREL using solar trackers (**Figure S6**). During a short-term experiment, the outdoor performance was stable at 58 mA sun^{-1} and virtually identical to the indoor performance at LBNL (Figure 3a). The long-term, outdoor stability was subsequently tested at

NREL on the same cell (Figure 3b). Despite the markedly different altitudes, local atmospheric characteristics and testing equipment, we were able to match the current at LBNL and NREL, when normalized by the fluctuating illumination intensity. During the three-day test at NREL, the peak current was stable around 60 mA sun^{-1}.

Every 90-120 minutes during the three days, the durability test was interrupted to measure the PV, EC and PEC performance separately via cyclic voltammetry (**Figure S7**), confirming the stability of the device. Additionally, we collected the water effluents and analyzed the aliquots of electrolyte every 90-120 minutes with inductively coupled plasma mass spectrometry (ICP-MS) to check for degradation products (**Figure S8**). On the cathode side, the measured Ga content was initially high, then drops down below the detection limit (3 ppt) of the ICP-MS instrument by Day 2. Indium is not detected during the testing period, suggesting that the source of Ga is III-V layer(s) that do not contain In or that In is retained within the IPEC cell. At the anode side, a constant but low release rate (approximately 1 – 2 ppb in every aliquot) of Ir into the electrolyte is observed over the whole testing period, indicating a slow loss of electrocatalyst from the anodic flowfield as expected from OER research.[52] The on-sun results highlight the capability of our device to consistently perform under various conditions, independent of the location, light source, and time.

2.5 Accelerated stress test

We previously reported stable performance for more than 100 hours of this IPEC architecture under liquid and vapor feed conditions.[23] Our findings led us to an understanding that water on the cathode side of the cell leads to accelerated degradation of the PV. Thus, in order to

accelerate water-induced degradation resulting from possible contact with the photovoltaic, liquid water was supplied to both sides of the cell and the degradation mechanisms were compared between 1 and 8 cm^2 cells. A four-day test was conducted indoors with a solar simulator at NREL to produce comparable and reproducible illumination and environmental conditions for the two cells. The initial current measured at NREL was similar to the LBNL results shown above, when the differences in solar simulator spectra are considered (**Figure S9**, Table 1), marking an important benchmark in reproducibility across different measurement locations. However, after showing a stable performance during our previous tests, the 1 and 8 cm^2 IPEC cells began to degrade under the harsher conditions (i.e. with water also fed through the cathode) at fairly constant rates of 0.60 mA cm^{-2} day^{-1} and 0.47 mA cm^{-2} day^{-1}, respectively (Figure 4a). The increased fluctuations in the measured current of the 8 cm^2 cell may be attributed to the much larger catalytic area partially losing contact to the membrane, or an irregularity in flow rate. Further scale-up may require thicker flowfield lands to increase mechanical stability or an optimized water-feed system. The authors note that the faradaic efficiency for H_2 was not determined during this stability test. However, a faradaic efficiency of ~0.95 for this IPEC architecture was recently reported by the authors.[23]

The daily cyclic voltammetry measurements clearly show that the degradation was PV-related in both cases as the PV short-circuit currents and fill factors dropped significantly over time while the EC performance remains stable (**Figure S10**). The PV degradation is highlighted by the intersection points of the PV and EC curves, which show a movement of the operating point towards lower currents while the operating voltage remains essentially stable or even

declines (Figure 4b). Furthermore, the high-frequency resistance of the cell's electrolyzer portion is stable, evidenced by electrochemical impedance spectroscopy (EIS, **Figure S11**).

2.6 Degradation analysis

Next, we systematically investigated the degradation of the PV. First, optical stereoscopy was employed on the 8 cm^2 PV cell after the durability tests without any disassembly (Error: Reference source not found and **Figure S12** for 1 cm^2 PV). The images show a color change of the top layers, attributable to thickness or refractive index changes, likely caused by water uptake of the epoxy. The structural change and blistering of the epoxy caused the gold grid fingers to delaminate and break (Figure S12). Factors influencing the adhesive stability of amine-crosslinked novolacs (the chemical platform in the epoxy used in this work) in contact with metal oxide surfaces are well-studied due to their importance in many applications.[53]–[56] Short-term failures such as those observed here can be attributed to interface chemistry and surface preparation. Ingress of water along the polymer-inorganic interface leads to stress corrosion cracking and adhesive failure either at the material interface, or in the region immediately adjacent to it depending on where fracture toughness is greater.[57] In the present work, adhesive failure seems to occur in part at the metal-oxide interface beneath the epoxy, indicating that the metal-epoxy adhesion is higher. Improved surface preparation using silane-based adhesion promoters and alternative cleaning techniques may reduce this failure mode. Longer-term failures arise when the epoxy degrades due to heating and illumination in the presence of oxygen.[58]–[61] Degradation can include hardening due to increased crosslinking, thermolysis at the higher end of the temperature range experienced on sun, formation of oxidation products that

increase hydrophilicity of the material, and plasticization by incorporated water. All of these would decrease the effectiveness of the encapsulant material over time, pointing to the need for improved encapsulants for at-scale technology deployments.

After carefully disassembling the IPEC cell, we employed a series of material characterization techniques to provide insight into the degradation mechanism of the PV upon epoxy failure, which in turn can lead to rational design of next generation materials for durable and efficient PEC devices. We first perform angle-resolved X-ray photoelectron spectroscopy (AR-XPS) on a pristine AZUR SPACE PV (8 cm^2) with an anti-reflective coating (ARC), compared to a pristine GaInP/GaAs PV from NREL (1 cm^2) without ARC as a reference sample that presents the as-prepared GaInP surface. The spectra of the AZUR PV only show signals from the top Al_2O_3 layer of the ARC,[62] while the In 3d and Ga 2p spectra show evidence for Ga-In-P bonding as well as In and Ga oxide peaks on the pristine NREL PV surface[63]–[65] (**Figure 6**a, 6e and **Figure S13-S15**). The ARC effectively masks any Ga or In signals on the pristine AZUR PV. In order to take a closer look at the surface composition, the penetration depth of XPS was reduced from ~4 to ~2 nm by choosing a takeoff angle of 60° relative to the surface normal instead of 0°. The resulting curves (Figure 6b and Figure S14-S15) show a dramatic increase of oxides compared to In and Ga in GaInP, indicating that the topmost surface is covered by native oxides in the absence of an ARC.

In order to examine the PV surface after the durability test, the protective epoxy coating is carefully peeled off after heating briefly on a hot plate at roughly 60 °C surface temperature. After the 4-day test, Ga and In peaks show up in the spectra of the AZUR PV, rather than only

observing Al_2O_3. However, only OH- and oxygen-bonded Ga and In are visible within the probing depth of XPS (Figure 6c and 6f). The Ga 2p and In 3d spectra show no evidence of bonding to P (Figure 6c, 6f and Figure S15c) when compared to the pristine NREL PV cell (Figure S14-S15), indicating that P is fully depleted within the top ~4 nm surface region. Furthermore, Ga and In oxide disappear when the incident beam angle is increased to 60°. Instead, only OH-bonding to Ga and In are observed for the top ~2 nm (Figure 6d and Figure S14b) and only a small amount of gallium oxide is measured when looking at the top 4 nm range (Figure 6c).[66]–[68] The intensity of the Al 2p signal from the Al_2O_3 ARC drops down significantly, with most of the residual Al-related species being aluminum hydroxide (Figure S13c). This is in line with the Pourbaix diagram, indicating that $AlOH^{2+}$ becomes the stable phase under operating conditions (Figure S13d).

Thus, the data suggest that during the durability testing, water penetrates through the epoxy via pinholes, and the corrosion starts by hydroxylation and dissolution of the alumina ARC. When the ARC is thin enough, water may reach the underlying GaInP causing its hydroxylation. It has been widely reported that the application of III-V compound semiconductors (*e.g.*, GaAs, InP and $GaInP_2$) in solar water splitting has been largely hampered due to their thermodynamic instability in a wide range of pH conditions.[69]–[72] We propose that the material corrodes in the form of $Ga(OH)_2^{+¿¿}$, $¿(OH)_2^{+¿¿}$ and $H_2PO_4^{-¿¿}$, as suggested by the Pourbaix diagram (Figure 6g),[73]–[75] while Ga_2O_3 could be relatively stable at a moderate pH operation point, passivating the surface and slowing down the corrosion process.[76]

SEM/EDS is further employed to locally track any surface changes after PEC testing with a larger field of view compared to XPS. We can see that the surface morphology remains similar

after the durability test (Figure 7 and **Figure S16**). In addition, the areal elemental mapping clearly shows the presence of GaInP, as shown in Figure 7. Given that the penetration depth of EDS is in the range of a few microns while XPS only probes the top few nanometers, the EDS results indicate that the bulk PV material is intact, while gradual hydroxylation and dissolution progresses as fresh material is exposed at the top.

3. Conclusion

To date, most PEC research focuses on the efficiency of small-scale cells (<1 cm^2), while scale-up and durability is an inevitable pathway for mass deployment of solar-fuel production. In this work, we develop a scalable framework for integration of highly efficient light-absorbers and state-of-the-art electrocatalysts and compare the performance and durability during scale-up. We perform tests on the same IPEC cell in two markedly different geographic locations, both indoors and outdoors to show the robustness of the design. The reproducibility is enabled in part by light source characterization and correction for spectral differences between the solar simulators. Furthermore, we are able to get consistent results across different cell sizes and PV materials. Significantly, our results show comparable stability between 1 and 8 cm^2 cell size, and suggest that performance and collection efficiencies scale with size. We find that water contact with the PV is detrimental to durability of the device, as it permeates the epoxy barrier layer and causes delamination of the grid fingers, as well as photocorrosion of the anti-reflective coating and GaInP light-absorber. The next step for optimization of this cell size or even larger scales is to improve the application of functional, catalytic anticorrosion layers, preventing mechanical damage caused by delamination.

4. Experimental

Catalyst Deposition

Pt and Ir are used as electrocatalysts for the hydrogen evolution (HER) and oxygen evolution (OER) reactions, respectively. These electrocatalysts are deposited by radio frequency (RF) sputtering onto the respective cathodic and anodic Ti flowfields. The flowfields are laser-cut from 100-µm-thick Ti foil, creating 100-µm-wide lands and 900-µm-wide channels with channel lengths of 17.3 mm. After machining, the Ti foils are solvent-cleaned by sequential sonication in acetone (BDH, semiconductor grade) and isopropanol (BDH, semiconductor grade), followed by rinsing with deionized water and drying under high purity N_2. Prior to sputter deposition, the Ti foils are further treated with Multi-Etch (Exotica Jewelry, Inc.), an alternative to hydrofluoric acid, to increase the active surface area and improve the adhesion between the catalyst and substrate. The as-etched flowfields are again rinsed with DI water, dried under N_2, and then immediately loaded into an AJA International 5-gun magnetron sputtering system for catalyst deposition.

The sputtering system is equipped with Pt (99.99%) and Ir (99.9%) targets made in-house at LBNL. Prior to sputter deposition, the substrates are cleaned by plasma etching at 15 W for 5 min in an Ar plasma at 30 mTorr. Immediately after this treatment, a 100 nm layer of catalyst is deposited by RF sputtering in a 3 mTorr atmosphere of Ar, at 150 W. The resulting thickness of deposited Ir and Pt is controlled by monitoring the sputter deposition rate with a quartz crystal. After deposition, the thickness is confirmed with a profilometer. The total amount of deposited catalyst per electrode corresponds to a loading of 0.2 mg cm^{-2}, and a total PGM loading of 0.4

mg cm^{-2}, which is one order of magnitude lower than a conventional PEM electrolyzer MEA, corresponding to 3-5 mg cm^{-2}.[8][77]

Commercial Photovoltaic

Commercially-available triple-junction III-V solar cells (Type: TJ Solar Cell 3T34C) from AZUR SPACE Solar Power GmbH with InGaP/GaAs/Ge sub-cells on a Ge substrate are used to drive the IPEC cell. The electrical data for that solar cell is available on the manufacturer's website.[29] The as-received cells (active area 30.18 cm^2) are diced into 1×1 cm^2 and 2×4 cm^2 pieces to fit into the endplates of the IPEC assembly. After dicing, the material is cleaned in a heated xylene bath at 50 °C, rinsed with isopropanol, then dried under flowing high-purity N_2. No edge passivation is applied, which leads to some reduction of power conversion efficiency relative to the as-received cell.

NREL Photovoltaic

The PV cells from NREL consist of a ~2.5-μm thick GaAs bottom subcell, an AlGaAs/GaAs tunnel junction interconnect, and a ~0.9-μm thick GaInP top subcell. Both subcells have a thin n^+-emitter and a thick p-base. The GaAs subcell is passivated on both sides by higher bandgap GaInP; the GaInP subcell is passivated by AlGaInP on the back and an AlInP window on the front.

The 1 and 8 cm^2 PV cells are grown by atmospheric pressure metalorganic vapor phase epitaxy (MOVPE), on a pair of custom-built reactors. The semiconductor layers are deposited on (001) zinc-doped GaAs substrates: for the 8 cm^2 cell the substrate is miscut 2° toward the (110) direction, whereas for the 1 cm^2 cell the substrate was miscut 4° toward the (111) direction.

Group-III elements are sourced from trimethylgallium (Ga), triethylgallium (Ga), trimethylindium (In) and trimethylaluminum (Al); Group-V elements are sourced from phosphine (P) and arsine (Ar). Hydrogen selenide (Se), disilane (Si), diethylzinc (Zn) and carbon tetrachloride (C) are the dopant sources.

The 8 cm^2 is grown on a full 2" wafer. The 1 cm^2 cell is grown on a cleaved portion of a wafer, that is prepped before growth by etching for 2 minutes in (2:1:10) $NH_4OH:H_2O_2:H_2O$. For the 8 cm^2 cell, the layers are grown at 650 °C, except for the tunnel junction and front contact layers that are grown at 600 °C. For the 1 cm^2 cell, the top cell is grown at 700 °C and the front contact at 650 °C. Growth rates range from 2.3-6.6 μm h^{-1}, as determined by calibration growths. The growth takes place in a purified hydrogen environment.

After growth, the samples are processed into a functioning device using standard cleanroom photolithography and wet-chemical etching techniques. A gold back contact is electroplated to the substrate, after cleaning for 30 seconds in (2:1:2) $NH_4OH:H_2O_2:H_2O$. Ni/Au grids and busbars are electroplated to the front contact through a Shipley 1818 photoresist mask. The grids are designed to be ~10 μm wide, ~2-3 μm tall, and spaced by ~1.1 mm. The devices are chemically isolated down to the substrate, and the front contact layer is etched away between the metal grids. Finally, the devices are cleaved from the surrounding substrate. The performance comparison between the 1 and 8 cm^2 PVs is shown in **Figure S17**.

Photovoltaic Mounting

The PV is mounted into a recessed ledge in the PMMA and secured on the backside along the edges of the PV, using a transparent two-component epoxy (EPO-TEK® 302-3M). A wire is

attached with Ag conductive glue to the back of the PV for current collection and is secured with more epoxy. Finally, the PV front is covered with the transparent epoxy to reduce corrosion at the PV surface, while carefully sustaining the electrical connection to the cathodic Ti flowfield.

Cell assembly

A mounting plate is used to assemble the components; the plate consists of a holder with four screws that protrude up and fit into the holes of the back endplate (PMMA raw material from McMaster-Carr Supply Company, Santa Fe Springs, CA). First, the back endplate is placed on top of the mounting table, which allows the entire cell to be aligned easily as the layers are stacked. Then, the silicone cathode gasket is centered on the back endplate, followed by the cathodic flowfield. An H^+-exchanged membrane (Nafion 115, 127 μm thick) is placed in between the cathodic and anodic flowfield, providing an electrically insulating layer. The membranes are used as received and assembled dry (equilibrated with environmental water vapor at room temperature, subsequently take up water upon introduction of liquid water or water vapor in the cell) in order to facilitate the assembly as wet membranes swell and curl. Next, the anode gasket is positioned on top of the anodic flowfield, followed by the front endplate. The cell is then compressed by tightening the eight screws evenly and in a star-shaped pattern to a final torque of 0.1 Nm. The gasket's thickness and endplate load is tuned in order to provide adequate active-area pressure but not damage the membrane by the lands of the Ti flowfields, confirmed with pressure film.[78] However, we emphasize that without the use of any gas-diffusion or porous-transport layers, whose opacity precludes their application, areas of the membrane are unsupported and thus affected by pressure differences.

Device performance measurements

All electrochemical, photoelectrochemical, and solid-state photovoltaic data are collected in two-electrode configuration, using a Biologic SP-300 potentiostat at LBNL and NREL. Cyclic voltammetry curves are obtained at scan rates of 20 mV s^{-1} for electrochemical characterizations and 50 mV s^{-1} for PV and PEC measurements. The electrochemical impedance is measured between 1-100,000 Hz with 6 points per decade. The design of this IPEC cell allows for current measurement between the PV back contact and the electrolyzer anode, while the operating voltage during stability measurements can be monitored between the PV front and back contacts.

Simulated sunlight is produced using an AAA-rated Newport Oriel Sol3A equipped with a Xe lamp and AM1.5G filter to obtain a 12″×12″ illumination area at LBNL. At NREL, a solar simulator from Abet Technologies (11000A-H) is used for indoor experiments. A Newport 91150V reference cell with a monocrystalline silicon solar cell (bandgap of 1.1 eV) and an integrated thermocouple is used to measure the solar irradiance at LBNL, while a calibrated GaInP cell (bandgap of 1.8 eV) is used as the primary calibration reference cell at NREL. The reference cells are calibrated and traceable to both NREL and to the International System of Units (SI). IPEC devices are positioned to receive 1 sun (1000 W m^{-2}) illumination to the PV front surface, as determined using the reference cells.

The reference cell calibration is done by setting the light intensity of the respective solar simulators to 1 sun according to the Si reference cell at LBNL and the GaInP reference cell at NREL. The remaining reference cells listed in Table 1 are then placed at the exact same position and the measured light intensity is recorded.

Solar trackers are employed to conduct outdoor measurements at LBNL (STR-22G Sun Tracker from EKO Instruments, Japan) and NREL (equatorial solar tracker from Eppley, USA).

At NREL, the outdoor light intensity is measured with a CMP22 pyranometer from Kipp & Zonen, located roughly 670 meters away from the PEC test station, while the light intensity at LBNL is obtained with the above-mentioned reference cell, mounted next to the IPEC cell on the solar tracker.

The cell temperature is measured with a thermocouple and is generally between 40-48 °C during indoor testing. During outdoor experiments, the temperature fluctuates between 20-48 °C, depending on the illumination conditions. A syringe pump is used to maintain continuous flow of water at a rate of 0.05 ml min^{-1} for 1 cm^2 and 0.4 ml min^{-1} for 8 cm^2 tests.

Surface characterizations

The surface chemical composition was characterized by XPS on a Kratos Axis Ultra DLD system at room temperature. A monochromatic Al Kα source (hν = 1486.6 eV) was used to excite the core level electrons of the material. Ga 2p, In 3d, P 2p, As 3d, O 1s, and C 1s core levels were collected, with a pass energy of 20 eV, step size of 0.05 eV, and 8 sweeps each to obtain a good signal-to-noise ratio. The measurement was performed at two takeoff angles, 0° and 60°, relative to the surface normal, to compare the bulk and surface composition. Spectral fitting was conducted using CasaXPS analysis software. Scanning electron microscopy (SEM) and energy dispersive X-ray spectroscopy (EDS) were performed in a FEI Quanta 250 FEG system to evaluate the surface morphology and composition.

Supporting Information

Supporting Information is available from the Wiley Online Library or from the author.

Acknowledgments

The authors thank Yalili Naranjo Chavez for her help with creating the Table of Contents image. The authors gratefully acknowledge research support from the HydroGEN Advanced Water Splitting Materials Consortium, established as part of the Energy Materials Network under the U.S. Department of Energy, Office of Energy Efficiency and Renewable Energy, Fuel Cell Technologies Office, under Contract Number DE-AC02-05CH11231. This work was supported in part by the U.S. Department of Energy, Office of Science, Office of Workforce Development for Teachers and Scientists (WDTS) under the Science Undergraduate Laboratory Internships Program (SULI). This work was authored in part by Alliance for Sustainable Energy, LLC, the manager and operator of the National Renewable Energy Laboratory for the U.S. Department of Energy (DOE) under Contract No. DE-AC36-08GO28308. Funding was provided by the U.S. Department of Energy, Office of Energy Efficiency and Renewable Energy, Hydrogen Fuel Cell Technologies Office (HFTO). The views expressed in the article do not necessarily represent the views of the DOE or the U.S. Government. The U.S. Government retains and the publisher, by accepting the article for publication, acknowledges that the U.S. Government retains a nonexclusive, paid-up, irrevocable, worldwide license to publish or reproduce the published form of this work, or allow others to do so, for U.S. Government purposes.

References

[1] F.W. Geels, B.K. Sovacool, T. Schwanen, S. Sorrell, *Science* **2017**, *357*, 1242.
[2] M. Kayfeci, A. Keçebaş, M. Bayat, in *Sol. Hydrog. Prod.*, Elsevier**2019**, 45.
[3] H. Dagdougui, R. Sacile, C. Bersani, A. Ouammi, *Hydrog. Infrastruct. Energy Appl. Elsevier Lond.* **2018**, 7.
[4] J.W. Vickers, H.N. Dinh, K. Randolph, A.Z. Weber, A.H. McDaniel, R. Boardman, T. Ogitsu, H. Colon-Mercado, D. Peterson, E.L. Miller, *ECS Trans.* **2018**, *85*, 3.

[5] B.A. Pinaud, J.D. Benck, L.C. Seitz, A.J. Forman, Z. Chen, T.G. Deutsch, B.D. James, K.N. Baum, G.N. Baum, S. Ardo, *Energy Environ. Sci.* **2013**, *6*, 1983.
[6] E.L. Miller, *Energy Environ. Sci.* **2015**, *8*, 2809.
[7] D. Jing, L. Guo, L. Zhao, X. Zhang, H. Liu, M. Li, S. Shen, G. Liu, X. Hu, X. Zhang, *Int. J. Hydrog. Energy* **2010**, *35*, 7087.
[8] M. Carmo, D.L. Fritz, J. Mergel, D. Stolten, *Int. J. Hydrog. Energy* **2013**, *38*, 4901.
[9] J. Jia, L.C. Seitz, J.D. Benck, Y. Huo, Y. Chen, J.W.D. Ng, T. Bilir, J.S. Harris, T.F. Jaramillo, *Nat. Commun.* **2016**, *7*, 1.
[10] D.M. Fabian, S. Hu, N. Singh, F.A. Houle, T. Hisatomi, K. Domen, F.E. Osterloh, S. Ardo, *Energy Environ. Sci.* **2015**, *8*, 2825.
[11] M.A. Modestino, S. Haussener, *Annu. Rev. Chem. Biomol. Eng.* **2015**, *6*, 13.
[12] A.C. Nielander, M.R. Shaner, K.M. Papadantonakis, S.A. Francis, N.S. Lewis, *Energy Environ. Sci.* **2015**, *8*, 16.
[13] S. Tembhurne, F. Nandjou, S. Haussener, *Nat. Energy* **2019**, *4*, 399.
[14] S. Tembhurne, F. Nandjou, S. Haussener, *Nat. Energy* **2019**, *4*, 399.
[15] M.M. May, H.-J. Lewerenz, D. Lackner, F. Dimroth, T. Hannappel, *Nat. Commun.* **2015**, *6*, 8286.
[16] W.-H. Cheng, M.H. Richter, M.M. May, J. Ohlmann, D. Lackner, F. Dimroth, T. Hannappel, H.A. Atwater, H.-J. Lewerenz, *ACS Energy Lett.* **2018**, *3*, 1795.
[17] J.L. Young, M.A. Steiner, H. Döscher, R.M. France, J.A. Turner, T.G. Deutsch, *Nat. Energy* **2017**, *2*, 1.
[18] R.C. Kainthla, B. Zelenay, J. Bockris, *J. Electrochem. Soc.* **1987**, *134*, 841.
[19] O. Khaselev, J.A. Turner, *Science* **1998**, *280*, 425.
[20] K.A. Walczak, G. Segev, D.M. Larson, J.W. Beeman, F.A. Houle, I.D. Sharp, *Adv. Energy Mater.* **2017**, 1602791.
[21] E. Verlage, S. Hu, R. Liu, R.J. Jones, K. Sun, C. Xiang, N.S. Lewis, H.A. Atwater, *Energy Environ. Sci.* **2015**, *8*, 3166.
[22] S. Hu, N.S. Lewis, J.W. Ager, J. Yang, J.R. McKone, N.C. Strandwitz, *J. Phys. Chem. C* **2015**, *119*, 24201.
[23] T.A. Kistler, D. Larson, K. Walczak, P. Agbo, I.D. Sharp, A.Z. Weber, N. Danilovic, *J. Electrochem. Soc.* **2019**, *166*, H3020.
[24] M. A. Modestino, M. Dumortier, S.M.H. Hashemi, S. Haussener, C. Moser, D. Psaltis, *Lab. Chip* **2015**, *15*, 2287.
[25] C. Xiang, Y. Chen, N. S. Lewis, *Energy Environ. Sci.* **2013**, *6*, 3713.
[26] S. Kumari, R.T. White, B. Kumar, J. M. Spurgeon, *Energy Environ. Sci.* **2016**, *9*, 1725.
[27] G. Heremans, C. Trompoukis, N. Daems, T. Bosserez, I.F. J. Vankelecom, J. A. Martens, J. Rongé, *Sustain. Energy Fuels* **2017**, *1*, 2061.
[28] T.A. Kistler, M.Y. Um, P. Agbo, *J. Electrochem. Soc.* **2020**, *167*, 066502.
[29] *AzurSpace* **n.d.**
[30] U. Babic, T.J. Schmidt, L. Gubler, *J. Electrochem. Soc.* **2018**, *165*, J3016.
[31] K.A. Walczak, G. Segev, D.M. Larson, J.W. Beeman, F.A. Houle, I.D. Sharp, *Adv. Energy Mater.* **2017**, *7*, 1602791.
[32] W.-H. Cheng, M.H. Richter, M.M. May, J. Ohlmann, D. Lackner, F. Dimroth, T. Hannappel, H.A. Atwater, H.-J. Lewerenz, *ACS Energy Lett.* **2018**, *3*, 1795.

[33] J.L. Young, M.A. Steiner, H. Döscher, R.M. France, J.A. Turner, T.G. Deutsch, *Nat. Energy* **2017**, *2*, 1.
[34] B. Turan, J.-P. Becker, F. Urbain, F. Finger, U. Rau, S. Haas, *Nat. Commun.* **2016**, *7*, 1.
[35] J.-P. Becker, B. Turan, V. Smirnov, K. Welter, F. Urbain, J. Wolff, S. Haas, F. Finger, *J. Mater. Chem. A* **2017**, *5*, 4818.
[36] A. Vilanova, P. Dias, J. Azevedo, M. Wullenkord, C. Spenke, T. Lopes, A. Mendes, *J. Power Sources* **2020**, *454*, 227890.
[37] W.J. Lee, P.S. Shinde, G.H. Go, E. Ramasamy, *Int. J. Hydrog. Energy* **2011**, *36*, 5262.
[38] Q. Zeng, J. Bai, J. Li, B. Zhou, Y. Sun, *Nano Energy* **2017**, *41*, 225.
[39] I.Y. Ahmet, Y. Ma, J.-W. Jang, T. Henschel, B. Stannowski, T. Lopes, A. Vilanova, A. Mendes, F.F. Abdi, R. van de Krol, *Sustain. Energy Fuels* **2019**, *3*, 2366.
[40] A. Hankin, F.E. Bedoya-Lora, C.K. Ong, J.C. Alexander, F. Petter, G.H. Kelsall, *Energy Environ. Sci.* **2017**, *10*, 346.
[41] S. Dilger, M. Trottmann, S. Pokrant, *ChemSusChem* **2019**, *12*, 1931.
[42] X. Yao, D. Wang, X. Zhao, S. Ma, P.S. Bassi, G. Yang, W. Chen, Z. Chen, T. Sritharan, *Energy Technol.* **2018**, *6*, 100.
[43] F.F. Abdi, R.R.G. Perez, S. Haussener, *Sustain. Energy Fuels* **2020**.
[44] C. Ottone, S. Hernández, M. Armandi, B. Bonelli, in *Test. Nov. Water Oxid. Catal. Sol. Fuels Prod.*, Springer**2019**, 93.
[45] W.J. Lee, P.S. Shinde, G.H. Go, E. Ramasamy, *Int. J. Hydrog. Energy* **2011**, *36*, 5262.
[46] I.Y. Ahmet, Y. Ma, J.-W. Jang, T. Henschel, B. Stannowski, T. Lopes, A. Vilanova, A. Mendes, F.F. Abdi, R. van de Krol, *Sustain. Energy Fuels* **2019**, *3*, 2366.
[47] V. Andrei, R.L. Hoye, M. Crespo-Quesada, M. Bajada, S. Ahmad, M. De Volder, R. Friend, E. Reisner, *Adv. Energy Mater.* **2018**, *8*, 1801403.
[48] M.R. Shaner, H.A. Atwater, N.S. Lewis, E.W. McFarland, *Energy Environ. Sci.* **2016**, *9*, 2354.
[49] C.A. Rodriguez, M.A. Modestino, D. Psaltis, C. Moser, *Energy Environ. Sci.* **2014**, *7*, 3828.
[50] A. Maljusch, M. Wullenkord, in *Adv. Photoelectrochem. Water Split.*, Royal Society Of Chemistry**2018**, 266.
[51] R. Sathre, J.B. Greenblatt, K. Walczak, I.D. Sharp, J.C. Stevens, J.W. Ager, F.A. Houle, *Energy Environ. Sci.* **2016**, *9*, 803.
[52] N. Danilovic, R. Subbaraman, K.-C. Chang, S.H. Chang, Y.J. Kang, J. Snyder, A.P. Paulikas, D. Strmcnik, Y.-T. Kim, D. Myers, V.R. Stamenkovic, N.M. Markovic, *J. Phys. Chem. Lett.* **2014**, *5*, 2474.
[53] S. Pletincx, L.L.I. Fockaert, J.M. Mol, T. Hauffman, H. Terryn, *Npj Mater. Degrad.* **2019**, *3*, 1.
[54] A. Amin, R. Sarkar, C.N. Moorefield, G.R. Newkome, *Polym. Eng. Sci.* **2013**, *53*, 2166.
[55] B. Salgin, Ö. Özkanat, J.M. Mol, H. Terryn, M. Rohwerder, *J. Phys. Chem. C* **2013**, *117*, 4480.
[56] T. Semoto, Y. Tsuji, K. Yoshizawa, *J. Phys. Chem. C* **2011**, *115*, 11701.
[57] P.A. Flinn, *MRS Bull.* **1995**, *20*, 70.
[58] E. Yousif, R. Haddad, *SpringerPlus* **2013**, *2*, 398.
[59] E.A. Sullivan, *J. Appl. Polym. Sci.* **1991**, *42*, 1815.

[60] L. Barral, J. Cano, J. Lopez, I. Lopez-Bueno, P. Nogueira, C. Ramirez, M.J. Abad, *J. Therm. Anal. Calorim.* **1998**, *51*, 489.
[61] V. Bellenger, J. Verdu, *J. Appl. Polym. Sci.* **1983**, *28*, 2677.
[62] R.-C. Fang, Q.-Q. Sun, P. Zhou, W. Yang, P.-F. Wang, D.W. Zhang, *Nanoscale Res. Lett.* **2013**, *8*, 92.
[63] X. Zhang, T.A. Pham, T. Ogitsu, B.C. Wood, S. Ptasinska, *J. Phys. Chem. C* **2020**, *124*, 3196.
[64] X. Zhang, S. Ptasinska, *Phys. Chem. Chem. Phys.* **2015**, *17*, 3909.
[65] R.J. Britto, J.D. Benck, J.L. Young, C. Hahn, T.G. Deutsch, T.F. Jaramillo, *J. Phys. Chem. Lett.* **2016**, *7*, 2044.
[66] J. Vigneron, M. Herlem, E.M. Khoumri, A. Etcheberry, *Appl. Surf. Sci.* **2002**, *201*, 51.
[67] X. Zhang, T.A. Pham, T. Ogitsu, B.C. Wood, S. Ptasinska, *J. Phys. Chem. C* **2020**, *124*, 3196.
[68] R.J. Britto, J.D. Benck, J.L. Young, C. Hahn, T.G. Deutsch, T.F. Jaramillo, *J. Phys. Chem. Lett.* **2016**, *7*, 2044.
[69] R.J. Britto, J.D. Benck, J.L. Young, C. Hahn, T.G. Deutsch, T.F. Jaramillo, *J. Phys. Chem. Lett.* **2016**, *7*, 2044.
[70] H. Lim, J.L. Young, J.F. Geisz, D.J. Friedman, T.G. Deutsch, J. Yoon, *Nat. Commun.* **2019**, *10*, 1.
[71] J.F. Carneiro, R.S. Rocha, P. Hammer, R. Bertazzoli, M.R.V. Lanza, *Appl. Catal. Gen.* **2016**, *517*, 161.
[72] E. Verlage, S. Hu, R. Liu, R.J. Jones, K. Sun, C. Xiang, N.S. Lewis, H.A. Atwater, *Energy Environ. Sci.* **2015**, *8*, 3166.
[73] A.K. Singh, L. Zhou, A. Shinde, S.K. Suram, J.H. Montoya, D. Winston, J.M. Gregoire, K.A. Persson, *Chem. Mater.* **2017**, *29*, 10159.
[74] K.A. Persson, B. Waldwick, P. Lazic, G. Ceder, *Phys. Rev. B* **2012**, *85*, 235438.
[75] A. Jain, I.E. Castelli, G. Hautier, D.H. Bailey, K.W. Jacobsen, *J. Mater. Sci.* **2013**, *48*, 6519.
[76] J.L. Young, K.X. Steirer, M.J. Dzara, J.A. Turner, T.G. Deutsch, *J. Mater. Chem. A* **2016**, *4*, 2831.
[77] N. Danilovic, K.E. Ayers, C. Capuano, J.N. Renner, L. Wiles, M. Pertoso, *ECS Trans.* **2016**, *75*, 395.
[78] M. Bernt, H.A. Gasteiger, *J. Electrochem. Soc.* **2016**, *163*, F3179.

Figures

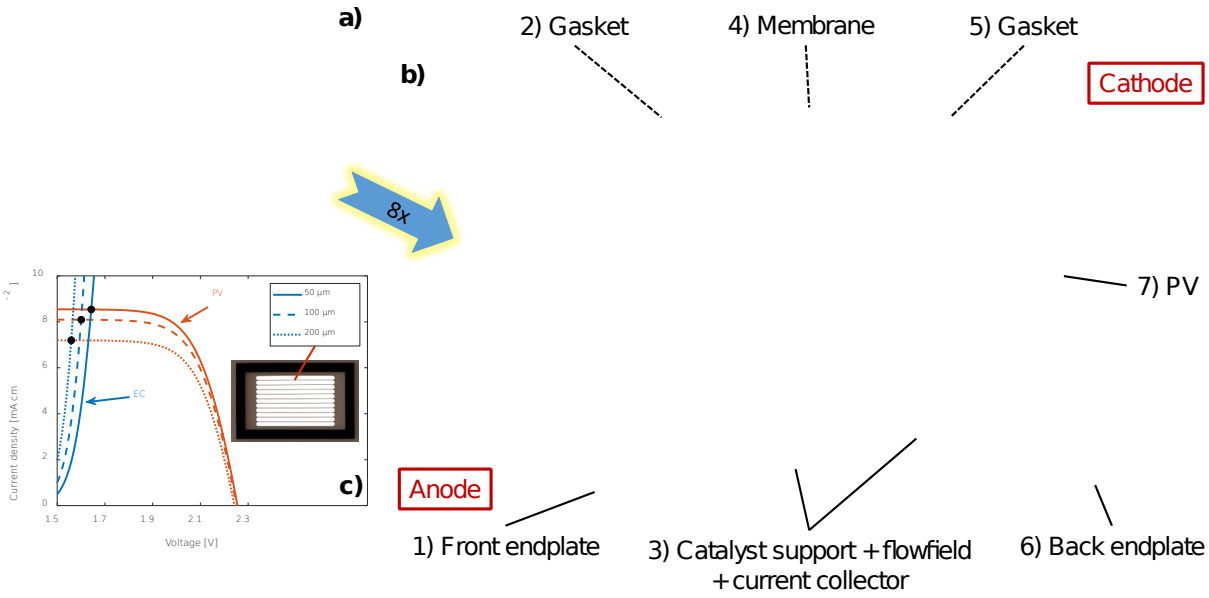

Figure 1. Integrated PEC (IPEC) cell design and optimization during the scale-up from a) 1 cm^2 to b) 8 cm^2. c) Modeling-driven design by optimizing the light-limited photocurrents through shading of the flowfield lands. The operating photocurrent is determined by the intersection of the electrochemical (EC) and PV performance curves. The intersections show the non-linear impact of the land width on the maximum photocurrent. The inset shows the center part of a flowfield with a land width of 100 µm and channel width of 900 µm.

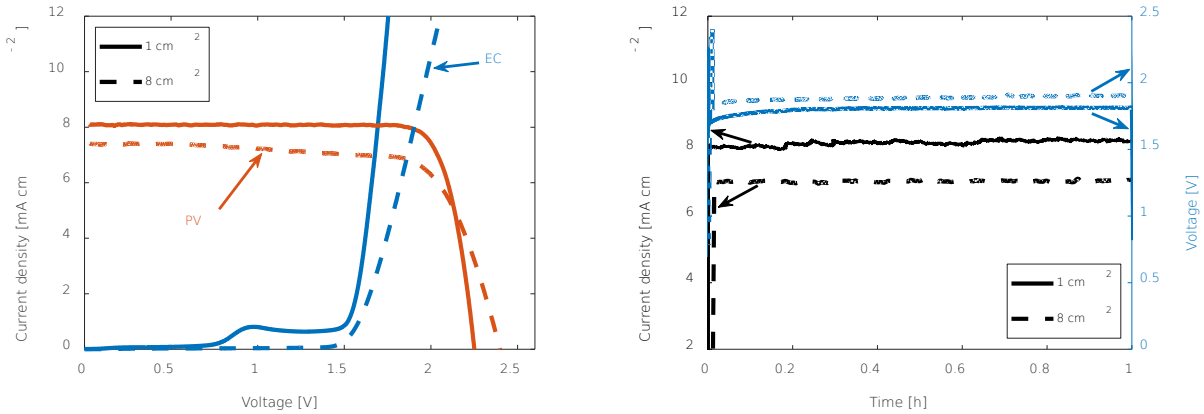

(a) (b)

Figure 2. Initial indoor performance of 1 and 8 cm^2 IPEC cells at LBNL, with NREL-made and commercial PVs, respectively. Both cells are operating with liquid water only on the anode side of the cell and all displayed current densities are based on the geometrical area of the PV. The illumination intensity is constant at 1 sun. a) Separate PV and EC curves, intersecting at the estimated operating point of the full IPEC assembly. b) One-hour stability test.

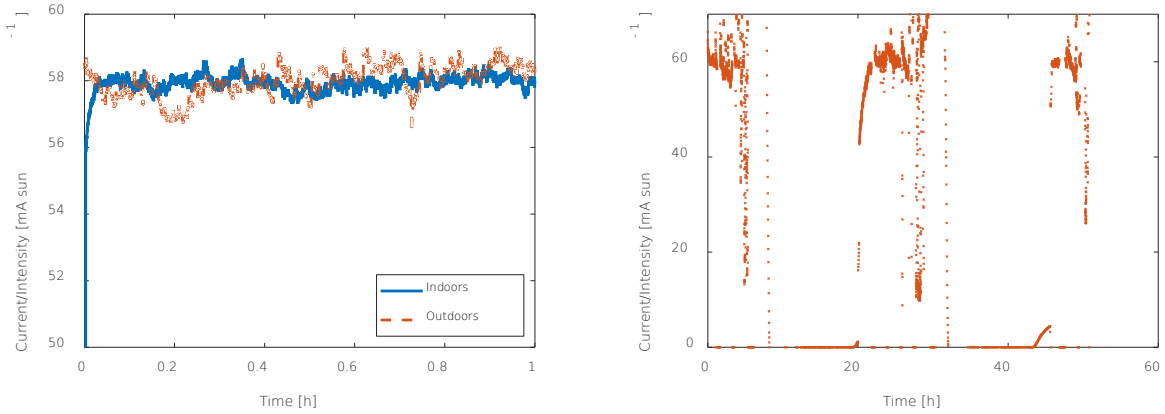

Figure 3. Outdoor tests with liquid water at the anode side of the cell. (a) Performance comparison of the 8 cm^2 AZUR SPACE PV in the IPEC assembly between indoor (room temperature, solar simulator) and outdoor (ambient air temperature, clear day) conditions at LBNL. (b) On-sun 8 cm^2 performance obtained at NREL over a three-day test. The weather was partially cloudy and the pyranometer measuring the illumination intensity was located ~670 m away from the test station, causing the spikes in the current during passing clouds. The cell temperature varies between 20-48 °C, depending on the illumination intensity.

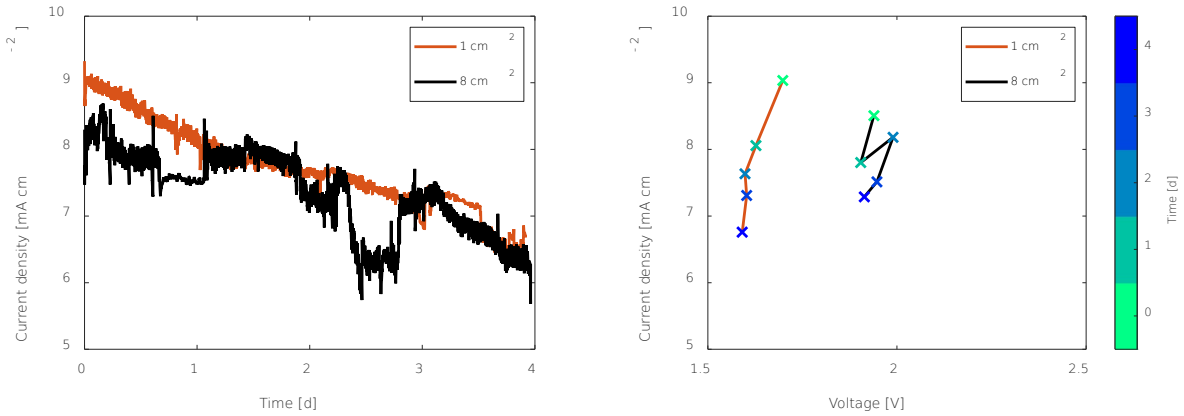

(a) (b)

Figure 4. Four-day indoor durability tests with 1 and 8 cm^2 IPEC cells at NREL. Liquid water is fed to the anode and cathode side of the cells and all displayed current densities are based on the geometrical area of the PV. (a) The photocurrent of both cells declines linearly over time. (b) The operating point of both cells, determined by the intersections of the PV and EC curves from Figure S10, moves towards lower currents at roughly the same voltage.

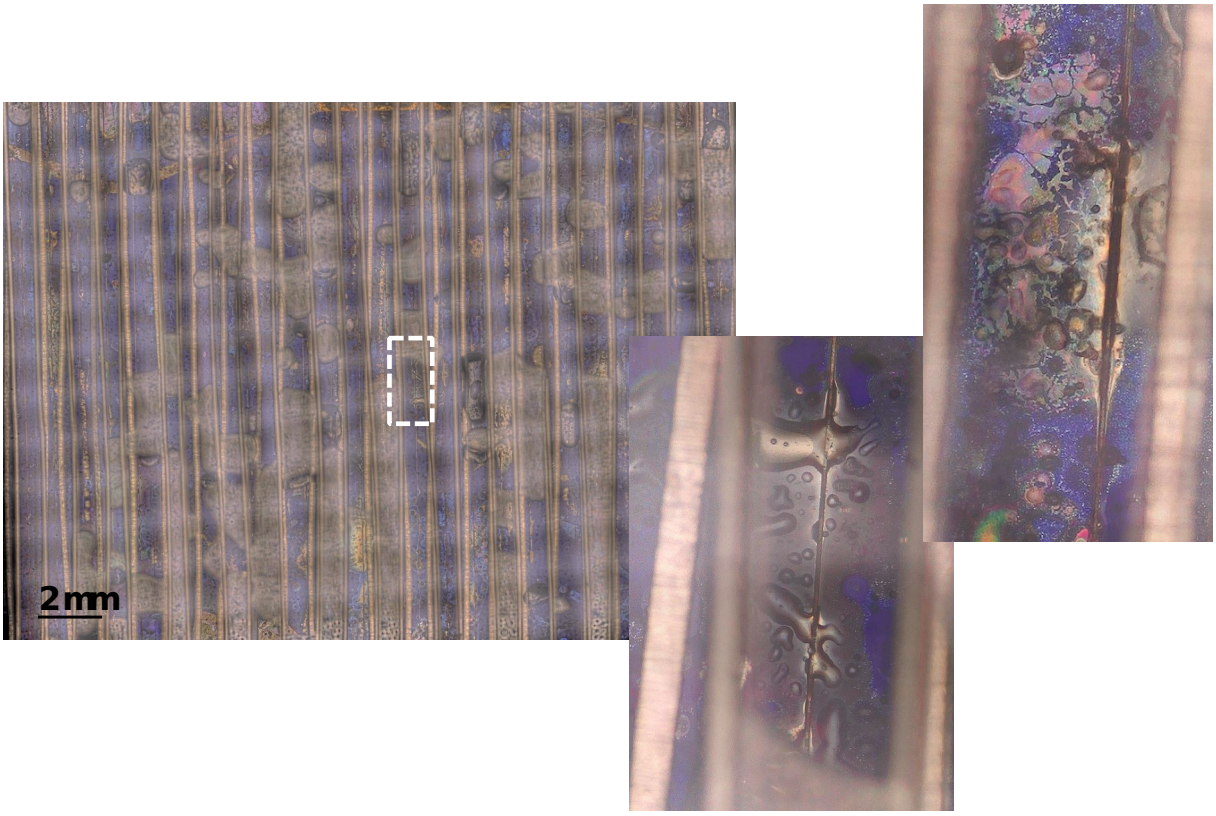

Figure 5. Stereoscopy of the 8 cm^2 IPEC cell after the 4-day accelerated degradation test, showing scattered discoloration of photoactive material. The white rectangular sections on the left are magnified on the right.

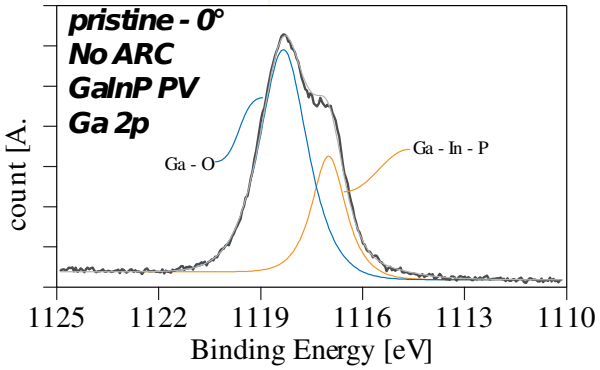
pristine - 0°
No ARC
GaInP PV
Ga 2p
Ga - O
Ga - In - P
count [A.
1125
1122
1119
1116
1113
1110
Binding Energy [eV]

(a)

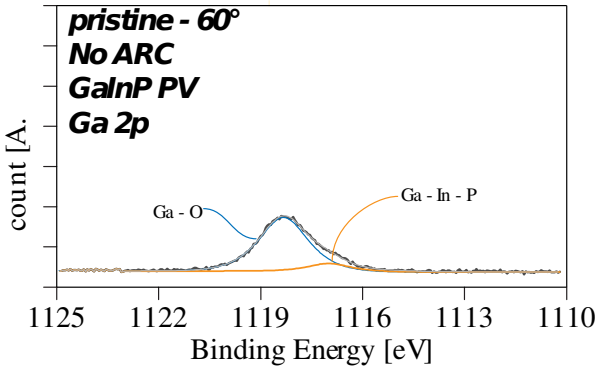
pristine - 60°
No ARC
GaInP PV
Ga 2p
Ga - O
Ga - In - P
count [A.
1125
1122
1119
1116
1113
1110
Binding Energy [eV]

(b)

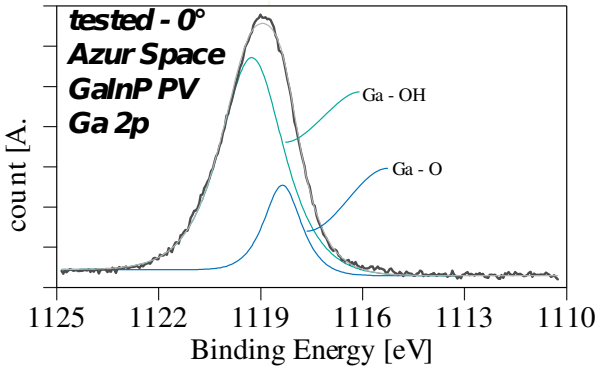
tested - 0°
Azur Space
GaInP PV
Ga 2p
Ga - OH
Ga - O
count [A.
1125
1122
1119
1116
1113
1110
Binding Energy [eV]

(c)

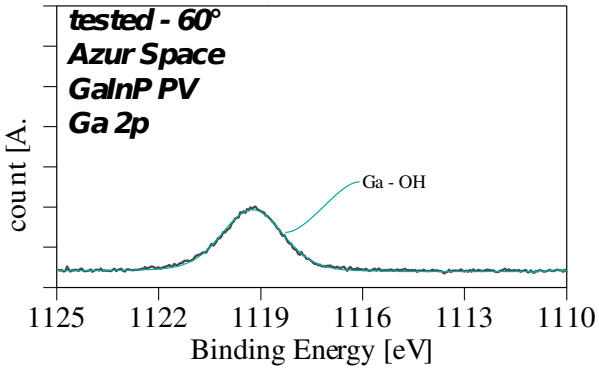
tested - 60°
Azur Space
GaInP PV
Ga 2p
Ga - OH
count [A.
1125
1122
1119
1116
1113
1110
Binding Energy [eV]

(d)

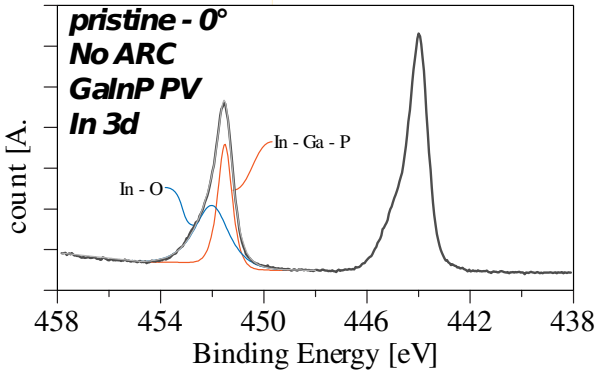
pristine - 0°
No ARC
GaInP PV
In 3d
In - Ga - P
In - O
count [A.
458
454
450
446
442
438
Binding Energy [eV]

(e)

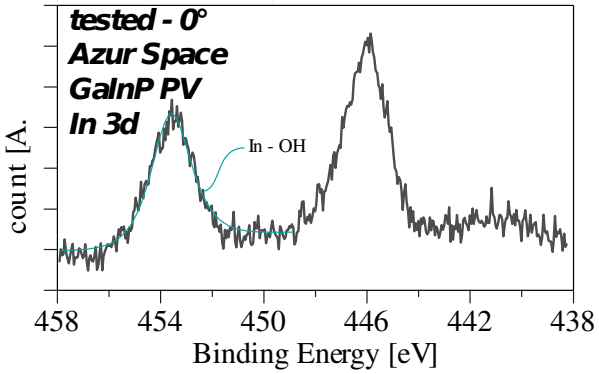
tested - 0°
Azur Space
GaInP PV
In 3d
In - OH
count [A.
458
454
450
446
442
438
Binding Energy [eV]

(f)

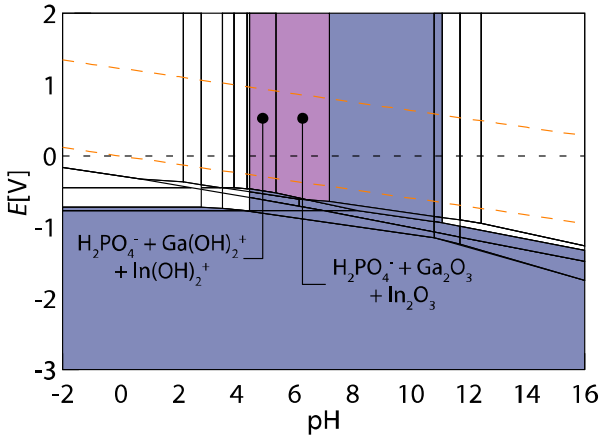

(g)

Figure 6. Degradation analysis using XPS. (a) Ga 2p core level XPS spectrum of the pristine GaInP/GaAs PV from NREL (1 cm^2) without ARC at a takeoff angle of 0° relative to the surface normal and (b) 60° relative to the surface normal; (c) Ga 2p core level XPS spectrum of the tested AZUR SPACE PV at a takeoff angle of 0° relative to the surface normal and (d) 60° relative to the surface normal; (e) In 3d XPS spectrum of pristine GaInP/GaAs PV from NREL (1 cm^2) without ARC and (f) tested AZUR SPACE PV at a takeoff angle of 0° relative to the surface normal; (g) the Materials Project Pourbaix diagram[73]–[75] of 25–25-50% Ga-In-P system in aqueous solution, assuming Ga, In and P ion concentrations of 10^{-8}, 10^{-7} and 10^{-5} mol kg^{-1}, respectively.

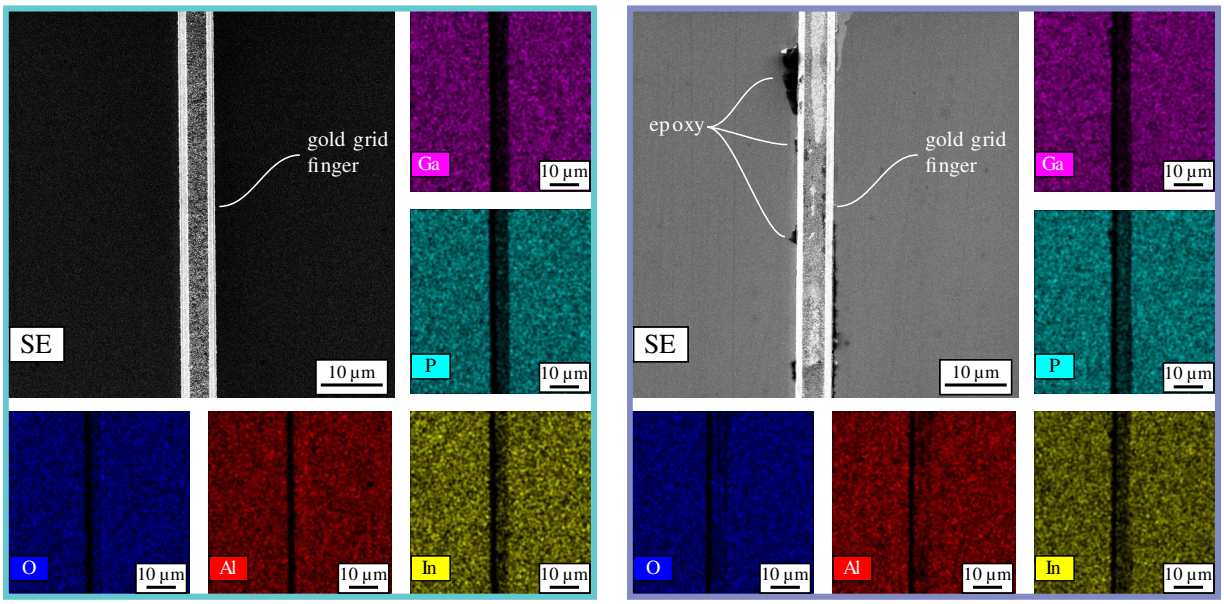

(a) (b)

Figure 7. SEM image of: (a) pristine AZUR SPACE PV cell and the corresponding areal elemental EDS mappings; (b) tested AZUR SPACE PV cell and the corresponding areal elemental EDS mappings.

Tables

Table 1. Summary of reference cell measurements on two solar simulators: ABET (NREL) and Sol3A (LBNL). The bandgap of the GaAs reference cell was closest to the current-limiting GaAs junction of our IPEC cells.

Reference cell	Bandgap [eV]	ABET [suns]	Sol3A [suns]
GaInP (primary)	1.8	1.00	1.07
GaInP (secondary)	1.8	1.00	1.07
AlGaAs	1.7	1.00	1.05
GaAs	1.4	**1.08**	**1.01**
InGaAs	1.2 (1.9 filter)	1.34	1.00
Si	1.1	1.18	1.00

Table of Contents

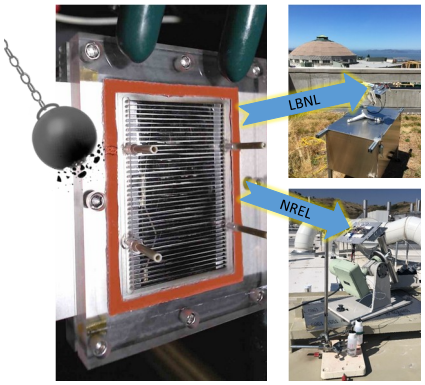

Photoelectrochemical (PEC) water splitting is an attractive method to produce CO_2 emission-free hydrogen fuel. However, most PEC devices are small, while lacking the durability and reproducibility necessary for commercial applications. This manuscript describes the scale-up of an integrated PEC (IPEC) platform from 1 to 8 cm^2, with repeatable measurement results and good durability at two markedly different locations.

ToC keyword: photoelectrochemical water splitting